ENGINEERING

Alkali metal halide–coated perovskite redox catalysts for anaerobic oxidative dehydrogenation of *n*-butane

Yunfei Gao[1,2]†, Xijun Wang[1,3]†, Noel Corolla[1], Tim Eldred[1], Arnab Bose[1], Wenpei Gao[1], Fanxing Li[1]*

Oxidative dehydrogenation (ODH) of *n*-butane has the potential to efficiently produce butadiene without equilibrium limitation or coke formation. Despite extensive research efforts, single-pass butadiene yields are limited to <23% in conventional catalytic ODH with gaseous O_2. This article reports molten LiBr as an effective promoter to modify a redox-active perovskite oxide, i.e., $La_{0.8}Sr_{0.2}FeO_3$ (LSF), for chemical looping–oxidative dehydrogenation of *n*-butane (CL-ODHB). Under the working state, the redox catalyst is composed of a molten LiBr layer covering the solid LSF substrate. Characterizations and ab initio molecular dynamics (AIMD) simulations indicate that peroxide species formed on LSF react with molten LiBr to form active atomic Br, which act as reaction intermediates for C—H bond activation. Meanwhile, molten LiBr layer inhibits unselective CO_2 formation, leading to 42.5% butadiene yield. The redox catalyst design strategy can be extended to CL-ODH of other light alkanes such as *iso*-butane conversion to *iso*-butylene, providing a generalized approach for olefin production.

INTRODUCTION

1,3-Butadiene is an important chemical in the manufacturing of synthetic rubbers, specialty plastics, and various other chemical products (*1*). The global 1,3-butadiene demand was 12 million metric tons in 2018 and is estimated to reach 15 million metric tons in 2023 (*2*). At present, 95% of 1,3-butadiene is produced as a by-product from steam cracking of naphtha and purified by a butadiene recovery process (*3*). However, steam cracking is highly energy and emission intensive. Moreover, 1,3-butadiene only represents 4 to 5 weight % (wt %) of the product from steam cracking of naphtha, with the major products being ethylene and propylene. As an alternative route for on-purpose production, 1,3-butadiene can be obtained from direct catalytic dehydrogenation (DH) of *n*-butane. However, this process faces several challenges such as high endothermicity (ΔH_r = 134 kJ/mol), limited selectivity, and severe coke formation (*1*).

Oxidative dehydrogenation of *n*-butane (ODHB) has been proposed to address the limitations in direct DH. ODHB has the advantage of being an exothermic reaction and requires lower reaction temperature (<500°C) (*1*). However, one of the most substantial challenges in *n*-butane ODH is the effectiveness for *n*-butane conversion and selective formation of 1,3-butadiene. As shown in Fig. 1A, conventional *n*-butane ODH catalysts include supported VO_x and/or MoO_x catalysts (*4*–*7*), and the 1,3-butadiene yields are generally limited to ~20%. Recently, modified oxygenated carbon nanotube (*8*), boron nitride, (*9*), and Mn+1AXn (MAX) phase materials (*10*) have also been reported for *n*-butane ODH, but the butadiene yields remain lower than 10% for these catalysts. Moreover, the use of gaseous O_2 in *n*-butane ODH leads to several other challenges: (i) Gaseous O_2 is costly and energy intensive to produce, and (ii) mixing *n*-butane and O_2 requires extensive safety precautions.

To address the disadvantages of *n*-butane ODH, a chemical looping strategy can be adopted (Fig. 1B). In short, chemical looping–ODH of *n*-butane (CL-ODHB) is carried out in two steps. Step 1 is an ODH reaction, where *n*-butane is selectively oxidized to butadiene and H_2O with the lattice oxygen from an oxide-based redox catalyst. Step 2 is air reoxidation, where the reduced metal oxide regains its lattice oxygen by reacting with gaseous oxygen in the air. This approach avoids direct contact between *n*-butane and air and does not require pure O_2 as a feedstock. As a novel approach especially for chemical production, chemical looping strategy has been explored for fossil fuel combustion (*11*, *12*), methane selective oxidation (*13*–*18*), ; thermochemical water/CO_2 splitting (*19*–*26*), air separation (*27*–*29*), and selective ODH of ethane, propane, and ethylbenzene (*30*–*36*). However, effective redox catalysts for *n*-butane ODH have yet to be reported, largely due to the high operating temperatures required, and hence low product selectivity, for typical chemical looping materials.

Molten salt has been used as an effective promoter for catalytic light alkane conversion. For example, Lercher and colleagues (*37*, *38*) reported that Dy_2O_3/MgO supported molten alkali metal chloride for ethane and propane ODH in the presence of gaseous O_2, and the active species were assigned to OCl^- ion. McFarland, Metiu, and colleagues (*39*–*42*) reported the use of molten halide salts for methane conversion and propane ODH. In this work, we report a molten LiBr covered $La_{0.8}Sr_{0.2}FeO_3$ (LSF@LiBr) redox catalyst for effective CL-ODHB. 1,3-Butadiene yields up to 42.5% were achieved at 500°C, far exceeding the previously reported values for O_2-cofeed butane ODH and butane ODH using lattice oxygen in terms of single-pass yield (Fig. 1A) at comparable or higher space-time yields (table S1). Detailed characterizations and computational studies indicated that the active lattice oxygen species within LSF oxidize the molten LiBr shell into atomic Br, as a reaction intermediate, for C—H bond activation of *n*-butane and 1-butene into butadiene product. Moreover, the molten LiBr layer inhibits unselective CO_2 formation.

RESULTS

Structural characterization of the redox catalyst

LSF@LiBr has a core-shell structure, where the core material is LSF and the shell material is LiBr. The surface enrichment of LiBr was

[1]North Carolina State University, Campus Box 7905, Raleigh, NC 27695-7905, USA. [2]Institute of Clean Coal Technology, East China University of Science and Technology, Shanghai 200237, China. [3]Department of Chemical and Biological Engineering, Northwestern University, Evanston, Illinois 60208, USA.
*Corresponding author. Email: fli5@ncsu.edu
†These authors contributed equally to this work.

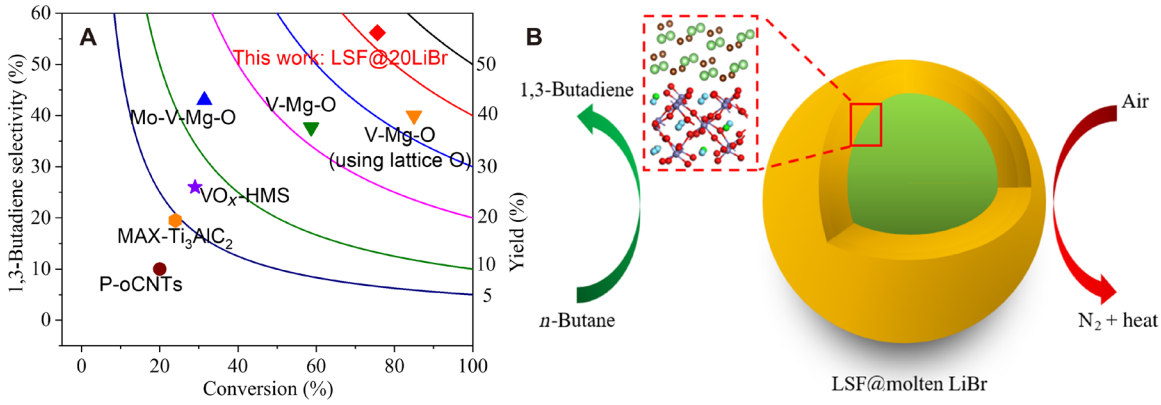

Fig. 1. Comparison of catalyst performance and schematic of the redox catalyst. (**A**) Comparison of reported *n*-butane ODH catalyst performance (*4*–*8*, *10*) and the CL-ODHB catalyst reported in this work. (**B**) Schematic of the CL-ODHB redox catalyst. P-oCNTs, phosphate modified oxygenated carbon nanotubes; HMS, hexagonal mesoporous silica.

first confirmed using x-ray photoelectron spectroscopy (XPS). As shown in Fig. 2A, LSF@LiBr samples are surface-enriched with Br, and all the LSF-related cations, i.e., Fe, Sr, and La, are suppressed. The atomic concentration of Li is not shown here because the XPS signal sensitivity to Li is poor. The surface enrichment of Br is further confirmed with energy-dispersive spectroscopy (EDS) in a scanning transmission electron microscope (STEM). As shown in Fig. 2B, the surface of the redox catalyst is enriched with Br, while the bulk is enriched with La, Sr, and Fe, consistent with the XPS results. The structure of LSF@LiBr under the working temperature (500°C) is further confirmed with in situ X-ray diffraction (XRD) (Fig. 2C), with temperature ramping from room temperature to 500°C under air. At room temperature, only LSF phase was observed. At 100°C, there appeared another phase, which can be assigned to lithium oxide bromide (Li_3OBr). Above 100°C, Li_3OBr phase disappeared and LiBr phase appeared. LSF phase was present throughout the temperature ramping program. The absence of crystallite LiBr phase at room temperature is likely to be due to the fact that LiBr tends to absorb moisture under air, forming amorphous lithium oxide hydrate. Above 460°C, LiBr phase disappeared due to the melting of surface LiBr. This was further confirmed with thermogravimetric analysis–differential scanning calorimetry (TGA-DSC) results in Fig. 2D. As shown in Fig. 2D, LSF@20LiBr has a heat absorption peak ranging from ~460° to 550°C, with a peak temperature at 513°C. This shows that surface LiBr is in a molten state at 500°C. It is noted that the melting point of surface LiBr is much lower than that of bulk LiBr (melting point = 552°C). As will be discussed in the following sections, the optimal working temperature of LSF@20LiBr is at 500°C. Thus, under the working temperature, the LSF core is covered with a layer of molten LiBr. A similar core-shell arrangement has been confirmed for LSF@10LiCl and LSF@10NaBr (fig. S1) and can also be inferred for other halide-modified LSF investigated in the current study.

Isothermal CL-BODH on modified LSF

Modifying LSF with a molten halide salt layer increases both *n*-butane conversion and 1,3-butadiene selectivity. As shown in Fig. 3A, unmodified LSF exhibited 71% butane conversion but only 2% 1,3-butadiene selectivity at 500°C. In fact, 93% of *n*-butane was converted into CO_x unselectively. In the meantime, it is noted that blank thermal conversion of *n*-butane at 500°C was minimal (~0.2%), and the thermally cracked products are mostly C_2 and C_3 products rather than 1,3-butadiene. Different promoters were applied to modify the LSF substrate for improved ODH performance. These promoters include LiBr, LiCl, KBr, NaBr, mixture of LiBr and LiCl, mixture of LiBr and KBr, and Li_2CO_3. It was determined that LiBr with 20% weight loading was the most effective. Up to 75.6% *n*-butane conversion and 56.2% 1,3-butadiene selectivity were obtained on LSF@20LiBr, corresponding to 42.5% 1,3-butadiene yield. Meanwhile, LiCl promoter, NaBr, and KBr promoters all exhibited lower conversions and selectivities. We also compared the commercial LSF substrate with LSF synthesized in-house, and they exhibited very similar performances (fig. S2). Other halogenated species such as C_4H_9Br was determined to be minimal at the product stream by measuring the mass/charge ratio (m/z) = 137 signal with a downstream quadrupole mass spectrometry (MKS Cirrus II) in fig. S3. The mass spectrometry data also confirmed minimal coke formation based on the negligible CO and CO_2 signals in the air reoxidation step. Figure 3B provides detailed product distributions and shows the cyclic stability of LSF@20LiBr with 20 CL-ODHB cycles. To determine whether the loss of LiBr by vaporization would be of a potential concern, LSF@20LiBr was treated at 500°C with argon gas for 15 hours in TGA. Figure S4 shows that the rate of LiBr loss is very slow (0.019 wt %/hour). This is consistent with the minimal deactivation observed within the 20 CL-ODHB cycles tested. The loss of LiBr during long-term operations can potentially be solved by bleeding in LiBr for replenishment from an engineering standpoint, similar to an industrial approach that replenishes HCl intermittently (*43*).

Active species and reaction pathway for CL-ODHB

The mechanism for the *n*-butane redox ODH and the effectiveness of molten LiBr layer were determined via both experimental and simulation studies. As shown in Fig. 3C, in situ XRD was conducted with *n*-butane redox ODH cycles at 500°C to determine the dynamic phase change of LSF@20LiBr. Although only the LSF phase can be observed at 500°C throughout the redox reactions, its lattice parameters were enlarged during the ODH (reduction) step as illustrated in Fig. 3C by the diffraction peak of the (110) plane. As can be seen, *n*-butane ODH on LSF caused the peak to slightly shift from 32.1° to 32.0°, and no other phase changes were observed. Reoxidation with air shifted the peak back to its original position. The cycle stability of phase structure was verified by running five redox cycles

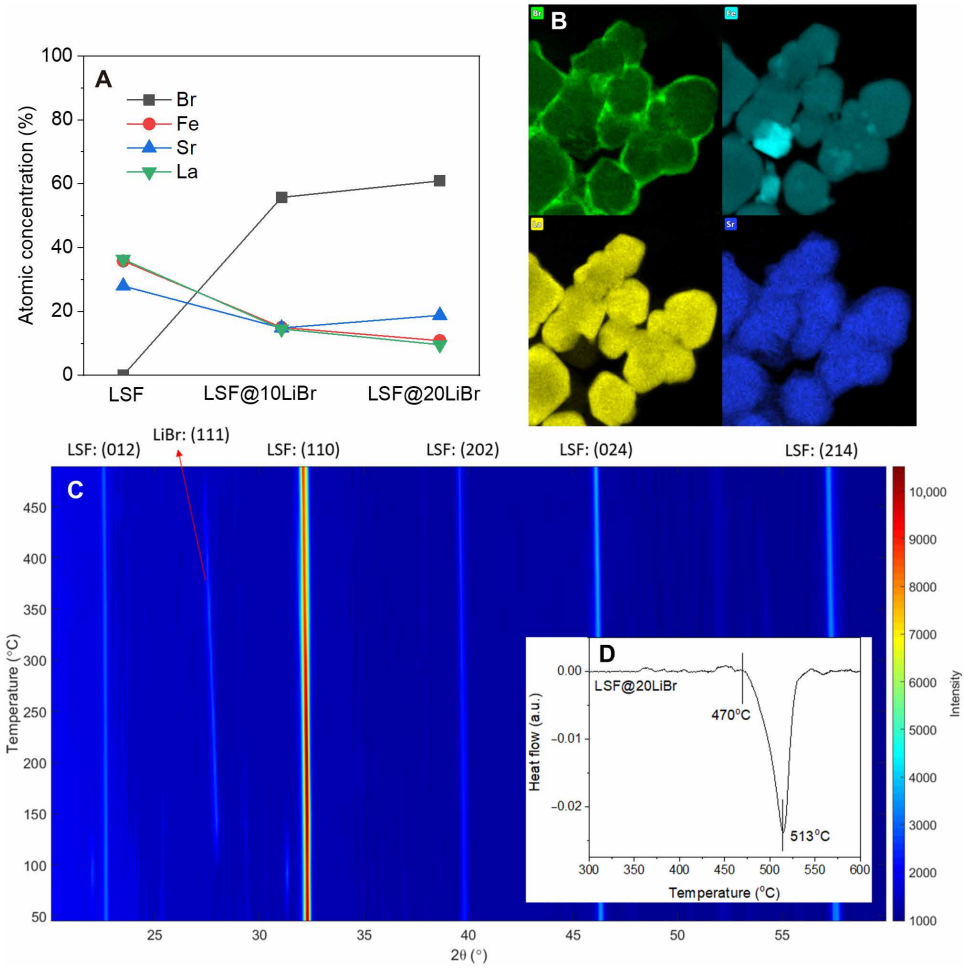

Fig. 2. Redox catalyst characterizations. (**A**) Surface atomic concentration obtained from XPS on LSF, LSF@10LiBr, and LSF@20LiBr. (**B**) STEM-EDS on LSF@20LiBr. (**C**) In situ XRD pattern on LSF@20LiBr with temperature ramping from room temperature to 500°C under air; the color intensity corresponds to the XRD peak intensity. (**D**) TGA-DSC on LSF@20LiBr to measure surface LiBr melting point on LSF. a.u., arbitrary units.

in the in situ XRD (fig. S5). On the basis of a previous study on an LSF@Li_2CO_3 redox catalyst in the context of ethane ODH, such a peak position transition corresponds to the transition between Fe^{4+} and Fe^{3+} oxidation state in LSF, and this would lead to evolution of active lattice oxygen into peroxide species in the form of Li_2O_2 (*30*). The presence of peroxide as active species also agrees with early studies of Lunsford and colleagues and more recent work using in situ characterizations for oxidative coupling of methane (*44*, *45*).

The interaction of Li_2O_2 and LiBr was further studied with ab initio molecular dynamics (AIMD). It was determined that it is energetically favorable for Li_2O_2 to oxidize LiBr into atomic Br, as shown in Fig. 4A. Furthermore, as shown by the AMID results of the evolution of Br_2 inside molten LiBr (Fig. 4B), the Br—Br bond cleaves to form two atomic Br after 1 ps and the equilibrated state at 18 ps showed an average Br—Br distance of 2.61 Å, larger than the bond length of Br_2(g) (2.28 Å). This showed that molecular Br_2 is unstable in molten LiBr and tends to decompose into two atomic Br. The atomic Br subsequently diffuses to the molten LiBr salt and gas interface to react with C_4H_{10}, producing butadiene in a stepwise fashion and forming HBr as a by-product (Fig. 4C). The as-formed HBr then reacts spontaneously with Li_2O and forms LiBr and H_2O, with $\Delta G = -202.2$ kJ/mol at 500°C (equivalent to 2.10 eV) calculated from HSC Chemistry 9. The reactions for the two half-cycles of CL-ODHB are summarized in Table 1. It is noted that these reactions are reversible, meaning that species such as Br and peroxide will be under a dynamic equilibrium. The reoxidation half-cycle can proceed via reactions (R) 1′ to 4′, as shown in Table 1. R1′ ($O_2 + 2Li_2O \Longleftrightarrow 2Li_2O_2$) has a ΔG of 58.5 kJ/mol at 500°C (equivalent to 0.60 eV) based on HSC, indicating that an appreciable O_2^{2-} concentration can present. Previous studies using density functional theory (DFT)–based thermodynamic calculations also suggested that Li_2O_2 is stable under high O_2 partial pressures (*46*). R2′ ($O_2 + 2LiBr \Longleftrightarrow Li_2O_2 + 2Br$) has a ΔG of 176.6 kJ/mol at 500°C (equivalent to 1.83 eV) based on HSC, showing that this reaction can also take place, albeit to a lesser extent. Metiu and colleagues (*42*) also suggested that alkali halide can be oxidized to peroxide based on AIMD calculations, although this study focused on the oxidation of LiI rather than LiBr. R3′ ($2Br + 2Li_2O \Longleftrightarrow Li_2O_2 + 2LiBr$) is the reverse reaction of R2 in the ODHB half-cycle. The evolved Li_2O_2 species in these reactions then react with LSF to reoxidize the Fe cation to a higher oxidation state, as has been reported previously (*30*). We also note that other supported catalysts besides LSF@20LiBr, such as $La_{0.8}Sr_{0.2}Fe_{0.8}Co_{0.2}O_3$@20LiBr

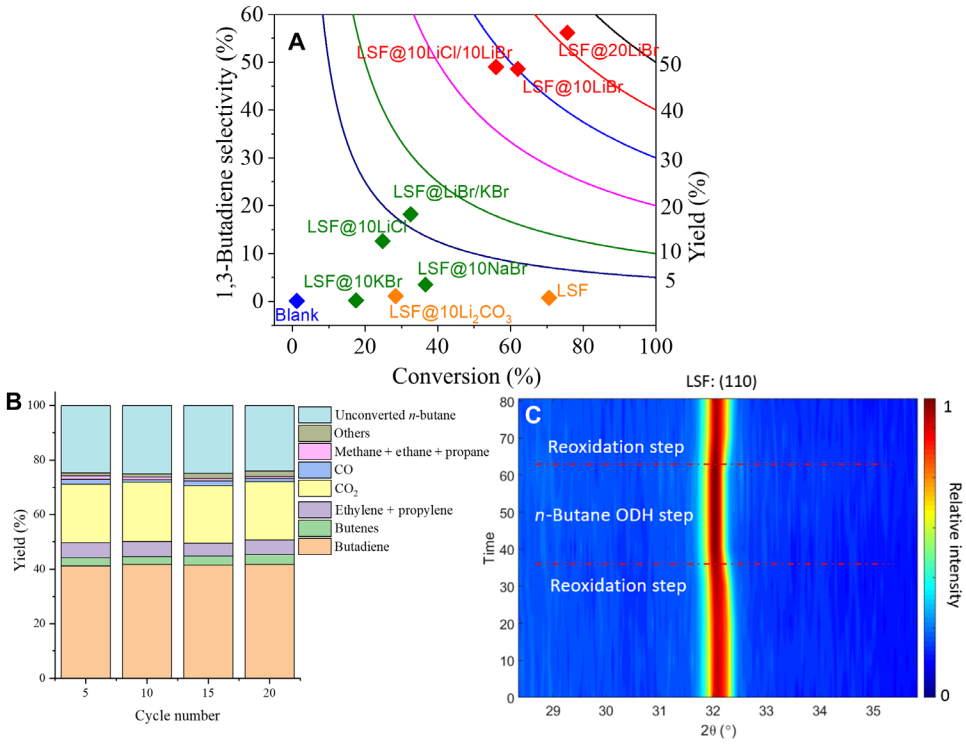

Fig. 3. Effect of redox catalyst compositions, product distributions, and in situ XRD. (**A**) CL-ODHB performance comparison of LSF, blank, and LSF with different promoters: temperature = 500°C and space velocity = 450 hours^{-1}. (**B**) Detailed product distributions showing carbon-based yields and 20 CL-ODHB cycles on LSF@20LiBr: temperature = 500°C and space velocity = 450 hours^{-1}; Butenes include 1-butene, *trans*-2-butene, and *cis*-2-butene; Others include propadiene, acetylene, *i*-butane, and C_{5+}. (**C**) In situ XRD on LSF@20LiBr under 500°C with *n*-butane ODH step and air reoxidation step.

Table 1. Summary of the key reactions in the ODH and reoxidation half-cycles (the complete CL-ODHB cycle has an overall reaction of $C_4H_{10}+O_2=C_4H_6+2H_2O$).

ODHB half-cycle
(1) $Li_2O + O_2^{2-}$ (of LSF) ⟺ $Li_2O_2 + O^{2-}$ (of LSF)
(2) $Li_2O_2 + 2LiBr \Longleftrightarrow 2Li_2O + 2Br$
(3) $C_4H_{10} + 2Br \Longleftrightarrow C_4H_8 + 2HBr$
(4) $C_4H_8 + 2Br \Longleftrightarrow C_4H_6 + 2HBr$ (note that reactions 3 and 4 are lumped reactions)
(5) $Li_2O + 2HBr \Longleftrightarrow 2LiBr + H_2O$
Overall reaction in the ODHB half-cycle: $C_4H_{10} + 2O_2^{2-}$ (of LSF) = $C_4H_6 + 2O^{2-}$ (of LSF) + $2H_2O$
Reoxidation half-cycle
(1)′ $O_2 + 2Li_2O \Longleftrightarrow 2Li_2O_2$
(2)′ $O_2 + 2LiBr \Longleftrightarrow Li_2O_2 + 2Br$
(3)′ $2Br + 2Li_2O \Longleftrightarrow Li_2O_2 + 2LiBr$ (reverse reaction of reaction 2)
(4)′ $Li_2O_2 + O^{2-}$ (of LSF) ⟺ $Li_2O + O_2^{2-}$ (of LSF) (reverse reaction of reaction 1)
Overall reaction in the reoxidation half-cycle: $O_2 + 2O^{2-}$ (of LSF) = $2O_2^{2-}$ (of LSF)

(LSFC@20LiBr) and $La_{0.8}Sr_{0.2}MnO_3$@20LiBr (LSM@20LiBr), can also catalyze CL-ODHB of butadiene. LSFC@20LiBr and LSM@20LiBr exhibited lower *n*-butane conversions, higher butene selectivities, and lower butadiene selectivities than LSF@20LiBr, indicating that the subsequent DH of butenes to butadiene is less pronounced in these redox catalysts (table S1).

Figure 4C shows that *n*-butane activation to butyl radical has a Gibbs free energy difference of 0.95 eV, while subsequent DH to 1-butene is much more energetically favorable (−1.47 eV). Similarly, 1-butene activation to butenyl radical has a free energy difference of 0.36 eV, whereas the subsequent butenyl radical DH to 1,3-butadiene is more favorable (−0.95 eV). It is noted that the first C─H bond dissociation energy for *n*-butane is around 400 kJ/mol or 4.15 eV (*47*), much higher than the Gibbs free energy difference with atomic Br. It has also been reported that halogens can be used as a "soft-oxidant" for oxidative methane coupling (*48*) and propane ODH (*41*, *42*). AIMD calculations also indicate that the desorption energies for C_4H_9 and C_4H_7 are 0.30 and 0.34 eV, respectively. Therefore, the as-formed radicals are more likely to be further dehydrogenated on the outer LiBr surface than being desorbed for gas-phase radical reactions (fig. S6). However, the as-formed 1-butene can be desorbed from the molten salt surface and re-adsorbed for further DH by Br, as will be discussed in the following section. The AIMD findings are also substantiated by gas-phase kinetics simulations via Reaction Mechanism Generator (RMG) and Chemkin-Pro: Given either gaseous

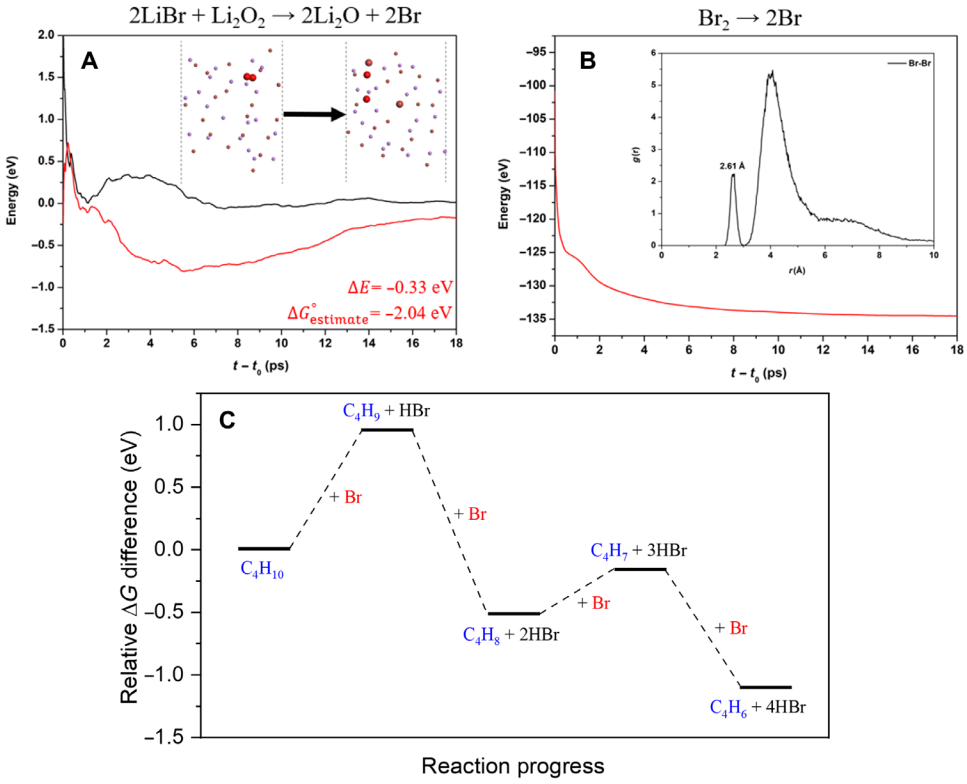

Fig. 4. ODH reaction pathway. AIMD calculation of (**A**) 2LiBr + Li_2O_2 ➔ 2Li_2O + 2Br and (**B**) Br_2 ➔ 2Br within LiBr molten salt. (**C**) *n*-C_4H_{10} reacting with Br-containing molten LiBr.

butyl radical or butenyl radical as the feedstock, 2-butene as opposed to butadiene is determined to be the primary product when the reaction proceeds exclusively through the gas-phase radical reaction pathway (fig. S7). In contrast, butadiene was the primary product observed experimentally (Fig. 3B). This confirms that *n*-butane and its dehydrogenated products, e.g., 1-butene, mainly reacted with atomic Br on the catalyst surface. A simple thermodynamic comparison was also conducted to determine the reason for lower activities of LiCl, NaBr, and KBr coatings. As summarized in table S3, from a thermodynamic standpoint, LiCl, NaBr, and KBr are all less favorable than LiBr to be oxidized into Cl or Br. The lack of halogen species in the molten shell would lead to low activity for *n*-butane activation.

To map out the reaction network, a "delplot" technique was further conducted to confirm the sequential C—H bond breakage of C_4H_{10} as predicted by AIMD (*49*). Figure 5A shows the delplot for unmodified LSF. As anticipated, the formation of CO_2 on unmodified LSF is more substantial than the formation of 1,3-butadiene and 1-butene. Nevertheless, it can be seen that the delplot for 1-butene has a negative slope and with a finite *y*-axis intercept, indicating that the formation of 1-butene is a primary reaction. Meanwhile, the delplot for 1,3-butadiene has a positive slope and with a *y*-axis intercept close to zero, indicating that the formation of 1,3-butadiene is a secondary reaction resulting from further ODH of 1-butene, consistent with the AIMD results. It is noted that the delplot of CO_2 has a positive slope and with a very large finite *y*-axis intercept. This indicates that CO_2 formation is both a primary reaction resulting from nonselective oxidation of *n*-butane and a secondary reaction resulting from secondary nonselective oxidation of 1-butene and 1,3-butadiene. This is more clearly demonstrated with the delplot of LSF@20LiBr. As can be seen in Fig. 5B, while similar trends hold true for the delplots of 1-butene and 1,3-butadiene, the delplot for CO_2 shows a larger positive slope at higher conversions but flats out at lower conversions into a finite *y*-axis intercept. This confirms that the formation of CO_2 is both a primary and secondary reaction. The fact that the CO_2 delplot *y*-axis intercept of LSF@20LiBr (*y*-axis intercept = 0.10) is much smaller than that of LSF (*y*-axis intercept = 0.52) but the slopes are similar at higher conversions could indicate that the primary CO_2 formation reaction was largely eliminated from the LiBr modification and that CO_x formation on LSF@20LiBr is mainly resulted from the oxidation of butane and butadiene products. A schematic drawing for the reaction pathway based on the delplot and the aforementioned characterization is shown in Fig. 5C. The delplot experiments are consistent with the space velocity effect tests on LSF@20LiBr, where higher space velocity leads to larger 1-butene selectivities and smaller 1,3-butadiene and CO_2 selectivities (table S4). The secondary conversion of butenes to butadiene is also verified with a 1-butene ODH experiment on LSF@20LiBr. Up to 98% 1-butene conversion can be achieved at 475°C with 65% 1,3-butadiene selectivity, leading to 63.6% 1,3-butadiene yield. More temperature effect tests on 1-butene ODH are shown in table S5.

Besides the delplot and activation energy experiments, the reaction order for CL-ODHB with LSF@20LiBr is studied by varying the feed partial pressure of *n*-butane. As shown in Fig. 5D, the formation rates of CO_2 and olefins are both linear with respect to *n*-butane partial pressure, indicating that they are both first-order reactions.

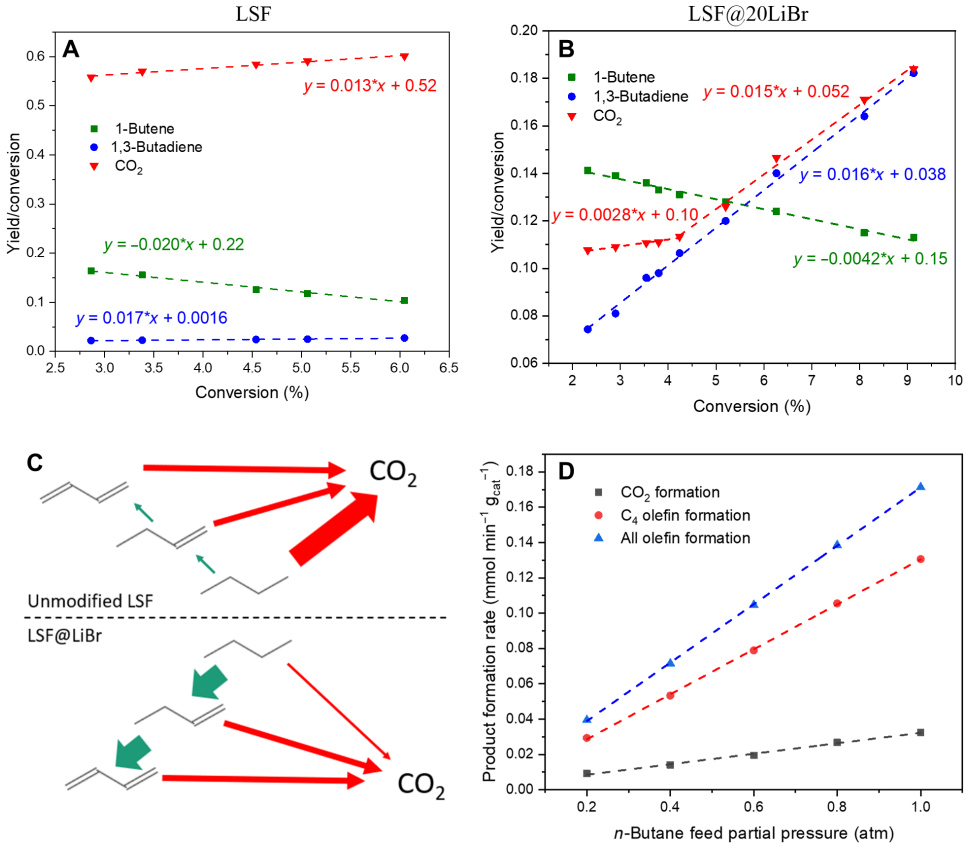

Fig. 5. ODH reaction network and reaction orders. Delplots for (**A**) unmodified LSF and (**B**) LSF@20LiBr. (**C**) Schematic drawing for reaction pathway network. The thickness of the lines qualitatively describes the extent of reaction. (**D**) Product formation rate versus *n*-butane feed partial pressure at 500°C with space velocity = 450 hours^{-1}.

As investigated by several studies, chemical looping oxidation can be considered as a modified Mars–van Krevelen reaction. For a Mars–van Krevelen reaction, the overall reaction rate is only approximated to first order to the gaseous hydrocarbon reactant when the partial pressure of gaseous oxygen (PO_2) is much larger than that for gaseous hydrocarbon reactant (P_R) (*50*, *51*). As chemical looping processes with lattice oxygen involvement are usually treated to exhibit a modified Mars–van Krevelen reaction mechanism (*52*), this shows that the participation of lattice oxygen is sufficiently fast and a high *n*-butane feed partial pressure is more beneficial for butadiene formation.

Inhibition of CO_2 formation by the molten LiBr layer

Molten LiBr layer not only induces atomic Br for butadiene formation but also inhibits CO_2 formation. This was examined with activation energy and pre-exponential factor measurements for CO_2 formation of LSF and LSF@LiBr in the kinetic regime (<20% conversion) with a higher space velocity (3600 hours^{-1}). As shown in Fig. 6A, unmodified LSF has an activation energy of 52.3 kJ/mol and pre-exponential factor of 12.1 s^{-1} for CO_2 formation. Meanwhile, LSF@20LiBr has an activation energy of 48.3 kJ/mol and a pre-exponential factor of 9.3 s^{-1} below the melting point temperature (~465°C). The lower pre-exponential factor of LSF@20LiBr than LSF below the melting point indicates unmelted LiBr that partly covers the unselective sites for CO_2 formation. In addition, the similar activation energy between LSF and LSF@LiBr below the melting point indicates that unmelted LiBr does not change the mechanism for CO_2 formation. The activation energy (86.6 kJ/mol) and pre-exponential factor (13.4 s^{-1}) of LSF@20LiBr are much higher above the melting point temperature. The high activation energy indicates that molten LiBr better covers the unselective sites and substantially inhibits CO_2 formation. Also, the high pre-exponential factor for CO_2 formation above the melting point temperature could be explained by higher active oxygen concentration in the LiBr melt, leading to higher collision frequency between hydrocarbons and active oxygen species.

The inhibition of CO_2 formation with LiBr layer was further studied with $^{18}O_2$ exchange experiments and H_2-TPR (temperature programmed reduction). As shown in Fig. 6B in $^{18}O_2$ exchange experiments on LSF and LSF@20LiBr, LSF exhibited significantly larger surface oxygen exchange rate than LSF@20LiBr in the temperature range investigated (450° to 600°C). The suppression of the surface oxygen exchange further leads to the suppressed lattice oxygen evolution as indicated by H_2-TPR in Fig. 6C. As can be seen, blank LSF exhibited lower temperature reduction peaks at 330° and 440°C, whereas LiBr-promoted LSF exhibited higher reduction peaks at 470° and 560°C. For LSF, the first reduction peak can be ascribed to the reduction of Fe^{4+} to Fe^{3+} and Fe^0, while the second reduction peak can be ascribed to the further reduction of Fe^{3+} to Fe^{2+} and Fe^0. For LSF@20LiBr, the first reduction peak can be ascribed to the reduction of Fe^{4+} and Fe^{3+} based on in situ XRD and prior

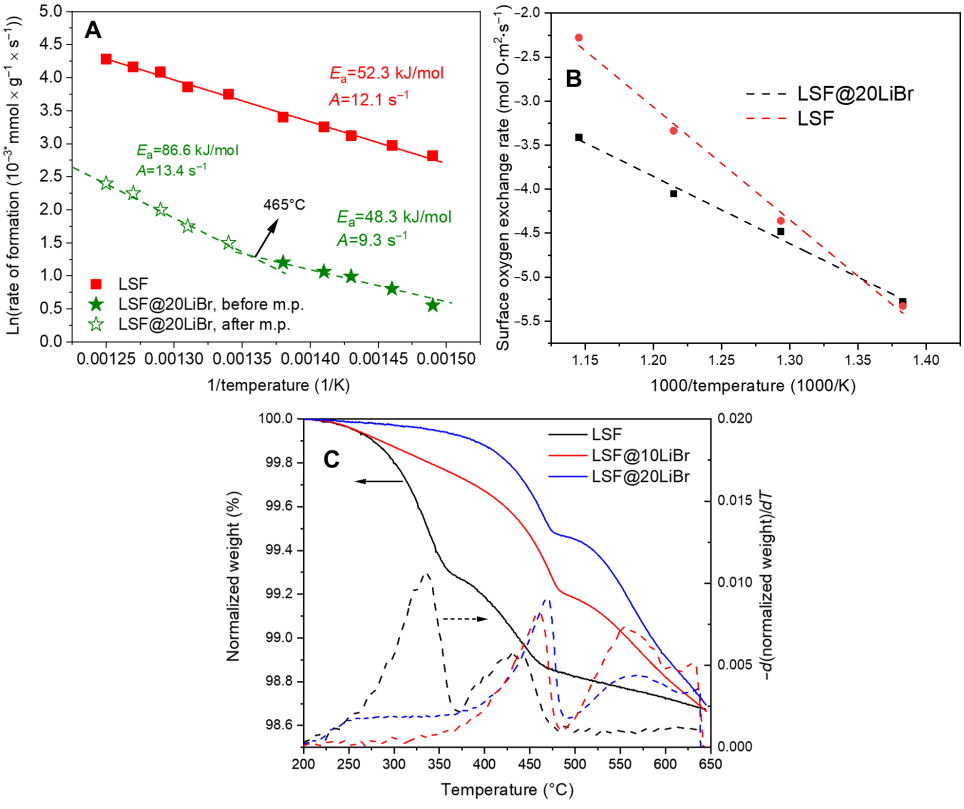

Fig. 6. Kinetic parameters and reducibility of the redox catalysts. (**A**) Activation energy and pre-exponential factor for CO_2 formation of LSF and LSF@20LiBr. (**B**) Surface oxygen exchange rate of LSF and LSF@20LiBr quantified with $^{18}O_2$ exchange experiment. (**C**) H_2-TPR of LSF and LSF@20LiBr. m.p., melting point.

reports (*30*). The prolonged mass decrease at higher temperatures is largely due to the inhibited reducibility of LSF by the molten salt. The slow vaporization of LiBr may also contribute to the weight loss, albeit to a minor extent. It is noted that the overall weight loss in H_2-TPR was nearly the same for blank LSF and LiBr-coated LSF, indicating that LiBr coating does not affect the overall lattice oxygen capacity of the LSF substrate.

Extension to chemical looping ODH of *iso*-butane

The LSF@LiBr redox catalyst can be extended for chemical looping *iso*-butane ODH to *iso*-butylene, and *iso*-butylene is a useful starting material for the synthesis of methyl tertiary butyl ether, methacrylates, and many other important chemical products (*9*). At 475°C, 51.0% *iso*-butane conversion and 43.3% *iso*-butylene selectivity were achieved, accounting for 22.2% *iso*-butylene yield. This exceeds most literature values for O_2-cofeed *iso*-butane ODH (Fig. 7) (*53*–*57*). The lower conversion and selectivity in *iso*-butane CL-ODHB than those in *n*-butane CL-ODHB are probably due to the lack of secondary conversion of 1-butene to 1,3-butadiene in *n*-butane CL-ODHB. More detailed product distributions with respect to temperature are shown in table S6. The promising *iso*-butylene yields indicate that the types of alkane feedstocks could be extended and LSF@LiBr is a general redox catalyst for chemical looping ODH of light alkanes.

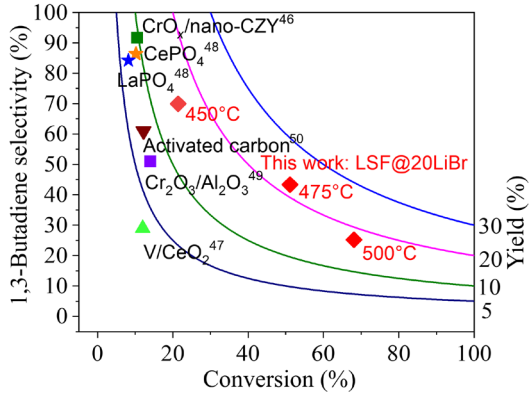

Fig. 7. Extension to *iso*-butane ODH applications. A comparison of reported *iso*-butane ODH catalyst performance (*53*–*57*) and the CL-ODHB catalyst reported in this work.

DISCUSSION

1,3-Butadiene is an important chemical building block. However, on-purpose butadiene production via catalytic DH of *n*-butane is equilibrium limited, energy intensive, and coke prone. ODHB has the potential to efficiently produce butadiene without equilibrium limitation or coke formation. Despite extensive research efforts, single-pass butadiene yields are limited to <23% in conventional catalytic ODH with gaseous O_2. Moreover, the use of gaseous oxygen requires costly air separation units and raises safety concerns.

This work focuses on anaerobic ODH by using the lattice oxygen species from a core-shell–structured "perovskite@molten LiBr" redox catalyst. The modified perovskite (LSF) is reduced with *n*-butane during the ODH step and then reoxidized with air via a cyclic redox

mode. By doing so, we integrate air separation with catalytic ODH while avoiding the direct contact between O_2 and *n*-butane. In this study, we demonstrated 42.5% butadiene yield, nearly doubling the maximum yield reported in literature. Experimental characterizations and AIMD simulations were carried out to determine the role of the molten LiBr shell, indicating that peroxide species formed on LSF react with molten LiBr to form atomic Br as effective reaction intermediates for C—H bond activation. The as-formed butyl radical is sequentially dehydrogenated to form 1-butene, butenyl radicals, and then butadiene as the final product. The mechanistic findings provide a generalized approach for anaerobic ODH of light hydrocarbons for olefin production, as validated by experimental results on efficient *iso*-butane ODH to *iso*-butylene.

Despite promising results, we did observe a slow (~0.019 wt %/hour) LiBr loss at high temperatures. This may cause the loss of butadiene selectivity over long-term operations. Further investigations on the effect of long-term LiBr loss and strategies for on-stream replenishment of the LiBr promoter would be important from a practical standpoint.

MATERIALS AND METHODS

CL-ODHB catalyst preparation

LSF was purchased from Praxair Surface Technologies. To synthesize halogen salt–coated LSF materials, an incipient wet impregnation method was applied. For example, to synthesize 20 wt % LiBr–coated LSF (LSF@20LiBr), 5 g of LSF was first weighed and placed into a beaker. Then, the calculated amount of LiBr (ACS reagent, ≥99.0%) was dissolved in 5 ml of deionized water and stirred to form a transparent solution. The solution was then placed onto LSF powders dropwise until it wetted the surface. The sample was then dried at 80°C. This procedure was repeated until all the LiBr solution has been added onto the LSF powder. The dried solids were then transferred into a ceramic sintering boat and sintered in a muffle furnace under air at 500°C for 5 hours.

As a comparison, in-house LSF was synthesized using a modified Pechini method. Stoichiometric amounts of $Fe(NO_3)_3{\cdot}9H_2O$ (98%; Sigma-Aldrich), $La(NO_3)_3{\cdot}6H_2O$ (99.9%; Sigma-Aldrich), and $Sr(NO_3)_2$ (99%; Noah Chemicals) were dissolved in deionized water with stirring at 30°C. Citric acid was then added to the solution at a 3:1 molar ratio to metal ions (Fe^{3+}, La^{3+}, and Sr^{2+}). The solution was stirred at 50°C for 0.5 hours to form a chelating solution. Ethylene glycol was then added to the solution to promote gel formation. The molar ratio between ethylene glycol and citric acid was 2:1. The solution was kept at 80°C with stirring until a viscous gel was formed. The gel was dried overnight at 130°C in a convection oven. The sample was then calcined in a tube furnace at 950°C for 12 hours under continuous air flow to form in-house LSF. The subsequent LiBr impregnation method was the same as in synthesis of commercial LSF@LiBr.

CL-ODHB catalyst characterization

The physiochemical properties of the CL-ODHB catalysts were characterized with XRD, XPS, STEM-EDS, and DSC. Ex situ XRD was measured with a Rigaku SmartLab x-ray diffractometer to analyze the crystalline phases of catalysts under room temperature, with a radiation source of monochromatic CuK_α ($\lambda = 0.1542$) and an operating condition at 40 kV and 44 mA. In situ XRD was measured with an Empyrean x-ray diffractometer in an Anton-Parr XRK-900 reactor chamber with a CuK_α ($\lambda = 0.1542$ nm) radiation source operated at 45 kV and 40 mA to generate XRD patterns under 500°C and under cyclic *n*-butane ODH and air reoxidation steps. XPS was measured with a nonmonochromatic MgK_α (1254 eV) excitation source to quantify the near-surface elemental composition. A PHOIBIS 150 hemispherical energy analyzer (SPECS GmbH) was used to record and generate XPS patterns. STEM-EDS was measured with a Thermo Fisher Scientific Titan 80-300 probe aberration–corrected STEM with monochromator equipped with a SuperX EDS system at Analytical Instrumentation Facility (AIF) at the North Carolina (NC) State University. DSC was measured with a thermogravimetric analyzer (TA Instruments, Q600) instrument. In DSC measurements, 50 mg of samples was placed in an Al_2O_3 crucible inside the thermogravimetric analyzer. Then, the system was heated up to 300°C with 5°C/min and held at 300°C for 1 hour under an Ar flow of 100 ml/min to remove moisture. Then, the system was further heated to 600°C with 5°C/min under an Ar flow of 100 ml/min, and the heat adsorption signal was recorded.

Oxygen exchange rate measurement

Oxygen exchange rates were measured using $^{18}O_2$ exchange experiments with a pulse experiment setup. A constant flow of 10% $^{16}O_2$ (50 ml min^{-1}, balance N_2) was used as the carrier gas, and pulses of 1 ml of 10% $^{18}O_2$ (balance He) were dosed onto samples for oxygen isotopic exchange. The detailed experimental setup and methodologies were reported by Bouwmeester *et al.* (*58*). A downstream quadrupole mass spectrometer (MKS Cirrus II) was used to record the signals for oxygen isotopes, namely, $^{16}O_2$, $^{16}O^{18}O$, and $^{18}O_2$. The quantification of these species was done by taking the integration of the characteristic peak mass 32, mass 34, and mass 36, respectively.

Reactive performance testing

The as-prepared CL-ODHB catalysts were first sieved into 180 to 800 μm. In a typical experiment, 4 g of the catalyst particles was loaded into a fixed bed quartz U-tube reactor with inner diameter (I.D.) = 1/8 inches. The reactor was then heated in a tubular furnace, with the testing temperature = 450° to 550°C. As an ODH step, 80 volume % of *n*-butane or *iso*-butane (Ar balance) was flown into the heated reactor for 15 s, with a total flow rate of 30 ml/min. The product distribution was monitored with a downstream gas chromatography (GC) (Agilent Technologies, 7890B) with a flame ionization detector (FID) channel for hydrocarbon analysis and two thermal conductivity detector (TCD) channels for H_2 and CO/CO_2. Then, the reactor was purged with Ar (30 ml/min) for 3 min. Next, 20 volume % of O_2 (Ar balance) was flown into the heated reactor with a flow rate of 30 ml/min as the air reoxidation step.

All the gaseous products in the ODHB step were collected using a gas bag, which was then analyzed by GC to obtain the overall product selectivity and yield over the entire ODHB half-cycle. Specifically, (i) the gas bag was connected to the downstream of the reactor 30 s before the start of the ODHB step; (ii) the gaseous products of the entire ODHB step were injected into the gas bag; (iii) the gas bag was connected for an additional 30 s to ensure that all the product gases are collected. The content of the gas bag was then injected into a GC sampling loop (Agilent Technologies, 7890B) with an FID channel for hydrocarbon analysis and two TCD channels to quantify H_2 and CO/CO_2. All species were quantified on the basis of calibrated peak area, and conversions, selectivities, and yields were calculated on the basis of these equations

$$n - \text{Butane conversion} = \frac{\text{Converted } n - \text{butane}}{\text{Feed } n - \text{butane}}$$

$$\text{Butadiene selectivity} = \frac{\text{Formed butadiene}}{\text{Converted } n - \text{butane}}$$

$$\text{Butadiene yield} = \frac{\text{Formed butadiene}}{\text{Feed } n - \text{butane}}$$

The selectivity and yield of other products (CO_x, butenes, etc.) were obtained in the similar approach.

Computational tools

AIMD simulations were carried out using the Vienna Ab Initio Simulation Package. DFT electronic energies and the forces acting on the atoms were calculated with the Perdew-Burke-Ernzerhof exchange correlation functional and the all-electron projector augmented wave model. The kinetic energy cutoff was set to 350 eV for the plane-wave expansion of the electronic wave function. The DFT-D3 method was applied to include van der Waals interaction corrections. All calculations were performed at the Gamma point, assuming spin-paired configurations.

The AIMD simulations for all the studied molten salt systems were performed at constant particle number, volume, and temperature, with a Nosé thermostat that keeps the temperature around 800 K, which is close to the experimental values (~573 K). The atomic motions were treated classically with a time step of 1 fs. The internal energies were calculated from the molecular dynamics simulations as the time average kinetic (E_{kin}) and potential energy (*42*)

$$\langle E \rangle_t = \frac{1}{t - t_0} \int_{t_0}^{t} (E_{DFT}(\tau) + E_{kin}(\tau))\, d\tau$$

where E_{DFT} and E_{kin} represent the DFT total energy and the classical kinetic energy, respectively. t_0 represents the cutoff time to allow the system to equilibrate. The motions before time t_0 were discarded such that the systems are sufficiently randomized to "forget" the initial conditions. The energies of the gas-phase molecules were calculated by fixing their center of mass, followed by adding $\frac{3}{2} k_B T$ as the translational contributions to the overall kinetic energy, where k_B is the Boltzmann constant. The estimated Gibbs free energy was calculated by $\Delta G^0_{estimate} = \Delta E + p\Delta V - T\Delta S^0_{estimate}$, where the volume change (ΔV) was assumed to originate purely from changes in the number of gas-phase molecules (Δn_{gas}) and is estimated by the ideal gas law ($p\Delta V = \Delta n_{gas} k_B T$). The entropies are obtained from the NIST-JANAF database (https://janaf.nist.gov/). Consistent with previous studies (*42*, *59*), zero-point energy (ZPE) corrections are not considered here because the required central processing unit time to accurately calculate the ZPE of tens of thousands of snapshots is prohibitively high.

Gas-phase thermoconversions for butyl and butenyl radicals were calculated via RMG-3.1.0 and Chemkin-Pro. To build a comprehensive reaction network, a tolerance factor of 0.01 was used in the RMG simulation using 90 volume % *n*-butane as feedstock (balance with Ar). The temperature was screened from 1000 to 1500 K, while the pressure was screened from 1 to 10 bar. To limit model size and avoid unreasonable products, the maximum carbon number was set as 8 and the maximum oxygen number was set as 4. After the model was build, Chemkin-Pro was used to simulate gas-phase kinetics with respect to reaction time using the zero-D batch reactor model. The condition for the simulation was set as 500°C and 1 atm, with 80 volume % butyl radical or butenyl radical as feedstock (balance with Ar). The residence time for the simulation was 1 s, and steady-state product distributions were achieved.

SUPPLEMENTARY MATERIALS

Supplementary material for this article is available at https://science.org/doi/10.1126/sciadv.abo7343

REFERENCES AND NOTES

1. L. M. Madeira, M. F. Portela, Catalytic oxidative dehydrogenation of *n*-butane. *Catal. Rev.* **44**, 247–286 (2002).
2. Global butadiene market—Segmented by application, end-user industry, and geography, growth, trends, and forecast (2019–2024); www.reportlinker.com/p05778169/Global-Butadiene-Market-Segmented-by-Application-End-user-Industry-and-Geography-Growth-Trends-and-Forecast.html?Utm:source=PRN?Utm:source=PRN [accessed July 2021].
3. W. C. White, Butadiene production process overview. *Chem. Biol. Interact.* **166**, 10–14 (2007).
4. M. Setnička, R. Bulánek, L. Čapek, P. Čičmanec, N-Butane oxidative dehydrogenation over VOX-HMS catalyst. *J. Mol. Catal. Chem.* **344**, 1–10 (2011).
5. X. Liu, L. Duan, W. Yang, X. Zhu, Oxidative dehydrogenation of n-butane to butenes on Mo-doped VMgO catalysts. *RSC Adv.* **7**, 34131–34137 (2017).
6. M. A. Chaar, D. Patel, M. C. Kung, H. H. Kung, Selective oxidative dehydrogenation of butane over V-Mg-O Catalysts. *J. Catal.* **105**, 483–498 (1987).
7. O. Rubio, J. Herguido, M. Menéndez, Oxidative dehydrogenation of *n*-butane on V/MgO catalysts—Kinetic study in anaerobic conditions. *Chem. Eng. Sci.* **58**, 4619–4627 (2003).
8. J. Zhang, X. Liu, R. Blume, A. Zhang, R. Schlögl, D. S. Su, Surface-modified carbon nanotubes catalyze oxidative dehydrogenation of *n*-butane. *Science* **322**, 73–77 (2008).
9. L. Shi, Y. Wang, B. Yan, W. Song, D. Shao, A.-H. Lu, Progress in selective oxidative dehydrogenation of light alkanes to olefins promoted by boron nitride catalysts. *Chem. Commun.* **54**, 10936–10946 (2018).
10. W. H. K. Ng, E. S. Gnanakumar, E. Batyrev, S. K. Sharma, P. K. Pujari, H. F. Greer, W. Zhou, R. Sakidja, G. Rothenberg, M. W. Barsoum, N. R. Shiju, The Ti_3AlC_2 MAX Phase as an efficient catalyst for oxidative dehydrogenation of *n*-butane. *Angew. Chem. Int. Ed. Engl.* **57**, 1485–1490 (2018).
11. C. Y. Lau, M. T. Dunstan, W. Hu, C. P. Grey, S. A. Scott, Large scale in silico screening of materials for carbon capture through chemical looping. *Energ. Environ. Sci.* **10**, 818–831 (2017).
12. M. Bui, C. S. Adjiman, A. Bardow, E. J. Anthony, A. Boston, S. Brown, P. S. Fennell, S. Fuss, A. Galindo, L. A. Hackett, J. P. Hallett, H. J. Herzog, G. Jackson, J. Kemper, S. Krevor, G. C. Maitland, M. Matuszewski, I. S. Metcalfe, C. Petit, G. Puxty, J. Reimer, D. M. Reiner, E. S. Rubin, S. A. Scott, N. Shah, B. Smit, J. P. M. Trusler, P. Webley, J. Wilcox, N. M. Dowell, Carbon capture and storage (CCS): The way forward. *Energ. Environ. Sci.* **11**, 1062–1176 (2018).
13. L. Zeng, Z. Cheng, J. A. Fan, L.-S. Fan, J. Gong, Metal oxide redox chemistry for chemical looping processes. *Nat. Rev. Chem.* **2**, 349–364 (2018).
14. V. L. Sushkevich, D. Palagin, M. Ranocchiari, J. A. van Bokhoven, Selective anaerobic oxidation of methane enables direct synthesis of methanol. *Science* **356**, 523–527 (2017).
15. Y. Liu, L. Qin, Z. Cheng, J. W. Goetze, F. Kong, J. A. Fan, L.-S. Fan, Near 100% CO selectivity in nanoscaled iron-based oxygen carriers for chemical looping methane partial oxidation. *Nat. Commun.* **10**, 5503 (2019).
16. S. Bhavsar, G. Veser, Chemical looping beyond combustion: Production of synthesis gas via chemical looping partial oxidation of methane. *RSC Adv.* **4**, 47254–47267 (2014).
17. Z. Cheng, D. S. Baser, S. G. Nadgouda, L. Qin, J. A. Fan, L.-S. Fan, C_2 selectivity enhancement in chemical looping oxidative coupling of methane over a Mg–Mn composite oxygen carrier by Li-doping-induced oxygen vacancies. *ACS Energy Lett.* **3**, 1730–1736 (2018).
18. X. Zhu, K. Li, L. Neal, F. Li, Perovskites as Geo-inspired oxygen storage materials for chemical looping and three-way catalysis: A perspective. *ACS Catal.* **8**, 8213–8236 (2018).
19. C. L. Muhich, B. W. Evanko, K. C. Weston, P. Lichty, X. Liang, J. Martinek, C. B. Musgrave, A. W. Weimer, Efficient generation of H2 by splitting water with an isothermal redox cycle. *Science* **341**, 540–542 (2013).
20. F. Donat, C. R. Müller, CO_2-free conversion of CH_4 to syngas using chemical looping. *Appl. Catal. Environ.* **278**, 119328 (2020).
21. D. Maiti, B. J. Hare, Y. A. Daza, A. E. Ramos, J. N. Kuhn, V. R. Bhethanabotla, Earth abundant perovskite oxides for low temperature CO_2 conversion. *Energ. Environ. Sci.* **11**, 648–659 (2018).

22. I. S. Metcalfe, B. Ray, C. Dejoie, W. Hu, C. de Leeuwe, C. Dueso, F. R. García-García, C.-M. Mak, E. I. Papaioannou, C. R. Thompson, J. S. O. Evans, Overcoming chemical equilibrium limitations using a thermodynamically reversible chemical reactor. *Nat. Chem.* **11**, 638–643 (2019).
23. Y. Ge, T. He, Z. Wang, D. Han, J. Li, J. Wu, J. Wu, Chemical looping oxidation of CH_4 with 99.5% CO selectivity over V_2O_3-based redox materials using CO_2 for regeneration. *AIChE J* **66**, e16772 (2020).
24. D. Sastre, C. Á. Galván, P. Pizarro, J. M. Coronado, Enhanced performance of CH_4 dry reforming over $La_{0.9}Sr_{0.1}FeO_3$/YSZ under chemical looping conditions. *Fuel* **309**, 122122 (2022).
25. S. Chuayboon, S. Abanades, S. Rodat, Solar chemical looping reforming of methane combined with isothermal H_2O/CO_2 splitting using ceria oxygen carrier for syngas production. *J. Energy Chem.* **41**, 60–72 (2020).
26. Z. Cao, X. Zhu, K. Li, Y. Wei, F. He, H. Wang, Moderate-temperature chemical looping splitting of CO_2 and H_2O for syngas generation. *Chem. Eng. J.* **397**, 125393 (2020).
27. J. Dou, E. Krzystowczyk, X. Wang, A. R. Richard, T. Robbins, F. Li, $Sr_{1-x}Ca_xFe_{1-y}Co_yO_{3-\delta}$ as facile and tunable oxygen sorbents for chemical looping air separation. *J. Phys. Energy* **2**, 025007 (2020).
28. J. Vieten, B. Bulfin, P. Huck, M. Horton, D. Guban, L. Zhu, Y. Lu, K. A. Persson, M. Roeb, C. Sattler, Materials design of perovskite solid solutions for thermochemical applications. *Energ. Environ. Sci.* **12**, 1369–1384 (2019).
29. T. Jia, E. J. Popczun, J. W. Lekse, Y. Duan, Effective Ca^{2+}-doping in $Sr_{1-X}Ca_xFeO_{3-\delta}$ oxygen carriers for chemical looping air separation: A theoretical and experimental investigation. *Appl. Energy* **281**, 116040 (2021).
30. Y. Gao, X. Wang, J. Liu, C. Huang, K. Zhao, Z. Zhao, X. Wang, F. Li, A molten carbonate shell modified perovskite redox catalyst for anaerobic oxidative dehydrogenation of ethane. *Sci. Adv.* **6**, eaaz9339 (2020).
31. S. Chen, L. Zeng, R. Mu, C. Xiong, Z.-J. Zhao, C. Zhao, C. Pei, L. Peng, J. Luo, L.-S. Fan, J. Gong, Modulating lattice oxygen in dual-functional Mo–V–O mixed oxides for chemical looping oxidative dehydrogenation. *J. Am. Chem. Soc.* **141**, 18653–18657 (2019).
32. L. M. Neal, V. P. Haribal, F. Li, Intensified ethylene production via chemical looping through an exergetically efficient redox scheme. *iScience* **19**, 894–904 (2019).
33. X. Zhu, Y. Gao, X. Wang, V. Haribal, J. Liu, L. M. Neal, Z. Bao, Z. Wu, H. Wang, F. Li, A tailored multi-functional catalyst for ultra-efficient styrene production under a cyclic redox scheme. *Nat. Commun.* **12**, 1329 (2021).
34. S. Chen, C. Pei, X. Chang, Z.-J. Zhao, R. Mu, Y. Xu, J. Gong, Coverage-dependent behaviors of vanadium oxides for chemical looping oxidative dehydrogenation. *Angew. Chem. Int. Ed. Engl.* **59**, 22072–22079 (2020).
35. X. Zhu, Q. Imtiaz, F. Donat, C. R. Müller, F. Li, Chemical looping beyond combustion—A perspective. *Energ. Environ. Sci.* **13**, 772–804 (2020).
36. Y. Gao, L. Neal, D. Ding, W. Wu, C. Baroi, A. M. Gaffney, F. Li, Recent advances in intensified ethylene production—A review. *ACS Catal.* **9**, 8592–8621 (2019).
37. C. P. Kumar, S. Gaab, T. E. Müller, J. A. Lercher, Oxidative dehydrogenation of light alkanes on supported molten alkali metal chloride catalysts. *Top. Catal.* **50**, 156–167 (2008).
38. C. A. Gärtner, A. C. van Veen, J. A. Lercher, Oxidative dehydrogenation of ethane on dynamically rearranging supported chloride catalysts. *J. Am. Chem. Soc.* **136**, 12691–12701 (2014).
39. D. C. Upham, Z. R. Snodgrass, C. Palmer, M. J. Gordon, H. Metiu, E. W. McFarland, Halogen-mediated partial combustion of methane in molten salts to produce CO_2-free power and solid carbon. *ACS Sustain. Chem. Eng.* **6**, 15673–15681 (2018).
40. D. C. Upham, H. H. Kristoffersen, Z. R. Snodgrass, M. J. Gordon, H. Metiu, E. W. McFarland, Bromine and iodine for selective partial oxidation of propane and methane. *Appl. Catal. Gen.* **580**, 102–110 (2019).
41. D. C. Upham, M. J. Gordon, H. Metiu, E. W. McFarland, Halogen-mediated oxidative dehydrogenation of propane using iodine or molten lithium iodide. *Catal. Lett.* **146**, 744–754 (2016).
42. C. Huang, H. H. Kristoffersen, X.-Q. Gong, H. Metiu, Reactions of molten LiI with I_2, H_2O, and O_2 relevant to halogen-mediated oxidative dehydrogenation of alkanes. *J. Phys. Chem. C* **120**, 4931–4936 (2016).
43. W. E. Ross, G. J. Carlson, Purification of metal halide catalyst in catalytic hydrocarbon conversions. U.S. Patent 2,421,524 (1947).
44. M. P. Rosynek, D. Dissanayake, J. H. Lunsford, Spectroscopic characterization of surface oxygen species on barium-containing methane coupling catalysts. *Stud. Surf. Sci. Catal.* **82**, 345–356 (1994).
45. K. Takanabe, A. M. Khan, Y. Tang, L. Nguyen, A. Ziani, B. W. Jacobs, A. M. Elbaz, S. M. Sarathy, F. Tao, Integrated in situ characterization of a molten salt catalyst surface: Evidence of sodium peroxide and hydroxyl radical formation. *Angew. Chem.* **129**, 10539–10543 (2017).
46. K. C. Lau, L. A. Curtiss, J. Greeley, Density functional investigation of the thermodynamic stability of lithium oxide bulk crystalline structures as a function of oxygen pressure. *J. Phys. Chem. C* **115**, 23625–23633 (2011).
47. L. A. Gribov, I. A. Novakov, A. I. Pavlyuchko, I. O. Kulago, B. S. Orlinson, "Spectroscopic" calculations of CH bond dissociation energies for ethane, propane, butane, isobutane, pentane, hexane, and neopentane using fundamental vibration frequencies. *J. Struct. Chem.* **44**, 961–969 (2003).
48. V. Paunović, J. Pérez-Ramírez, Catalytic halogenation of methane: A dream reaction with practical scope? *Catal. Sci. Technol.* **9**, 4515–4530 (2019).
49. N. A. Bhore, M. T. Klein, K. B. Bischoff, The delplot technique: A new method for reaction pathway analysis. *Ind. Eng. Chem. Res.* **29**, 313–316 (1990).
50. M. A. Vannice, An analysis of the Mars–van Krevelen rate expression. *Catal. Today* **123**, 18–22 (2007).
51. P. Mars, D. W. Van Krevelen, Oxidations carried out by means of vanadium oxide catalysts. *Chem. Eng. Sci.* **3**, 41–59 (1954).
52. A. Shafiefarhood, J. C. Hamill, L. M. Neal, F. Li, Methane partial oxidation using FeO_x @$La_{0.8}Sr_{0.2}FeO_{3-\delta}$ core–shell catalyst—Transient pulse studies. *Phys. Chem. Chem. Phys.* **17**, 31297–31307 (2015).
53. G. Wang, H. Dai, L. Zhang, J. Deng, C. Liu, H. He, C. T. Au, CrO_x/*nano*-$Ce_{0.60}Zr_{0.35}Y_{0.05}O_2$ catalysts that are highly selective for the oxidative dehydrogenation of isobutane to isobutene. *Appl. Catal. A Gen* **375**, 272–278 (2010).
54. Z. Wu, V. Schwartz, M. Li, A. J. Rondinone, S. H. Overbury, Support shape effect in metal oxide catalysis: Ceria-nanoshape-supported vanadia catalysts for oxidative dehydrogenation of isobutane. *J. Phys. Chem. Lett.* **3**, 1517–1522 (2012).
55. Y. Takita, K. Sano, T. Muraya, H. Nishiguchi, N. Kawata, M. Ito, T. Akbay, T. Ishihara, Oxidative dehydrogenation of iso-butane to iso-butene II. Rare earth phosphate catalysts. *Appl. Catal. A Gen.* **170**, 23–31 (1998).
56. B. Grzybowska, J. Słoczyński, R. Grabowski, K. Wcisło, A. Kozłowska, J. Stoch, J. Zieliński, Chromium oxide/alumina catalysts in oxidative dehydrogenation of isobutane. *J. Catal.* **178**, 687–700 (1998).
57. J. J. D. Velásqueza, L. M. C. Suárez, J. L. Figueiredo, Oxidative dehydrogenation of isobutane over activated carbon catalysts. *Appl. Catal. Gen.* **311**, 51–57 (2006).
58. H. J. Bouwmeester, C. Song, J. Zhu, J. Yi, M. van Sint Annaland, B. A. Boukamp, A novel pulse isotopic exchange technique for rapid determination of the oxygen surface exchange rate of oxide ion conductors. *Phys. Chem. Chem. Phys.* **11**, 9640–9643 (2009).
59. D. C. Upham, V. Agarwal, A. Khechfe, Z. R. Snodgrass, M. J. Gordon, H. Metiu, E. W. McFarland, Catalytic molten metals for the direct conversion of methane to hydrogen and separable carbon. *Science* **358**, 917–921 (2017).

Acknowledgments: We acknowledge the use of the AIF at the NC State University. **Funding:** This work was supported by the U.S. NSF (award no. CBET- 2116724), the DOE-RAPID Institute (DE-EE007888-05-6), and the Kenan Institute for Engineering, Technology and Science at the NC State University. **Author contributions:** F.L. conceived and supervised the study. Y.G. and F.L. wrote the manuscript. Y.G. and N.C. carried out the experiments and characterizations. X.W. carried out the DFT simulations. T.E. and W.G. conducted the STEM-EDS measurements. A.B. conducted the RMG and Chemkin-Pro simulations. **Competing interests:** The authors declare that they have no competing interests. **Data and materials availability:** All data needed to evaluate the conclusions in the paper are present in the paper and/or the Supplementary Materials.

Submitted 25 February 2022
Accepted 13 June 2022
Published 27 July 2022
10.1126/sciadv.abo7343